separations

MDPI

Article

Enhanced Removal of Sulfonamide Antibiotics by Spent Coffee Ground-Derived Biochars Produced Under a CO_2 Atmosphere

Wenting Li, Xian Yuan, Binrong Li and Xiaofang Shen *

School of Environmental Science and Engineering, Suzhou University of Science and Technology, Suzhou 215009, China; liwenting2020@outlook.com (W.L.); yuanxian1004@outlook.com (X.Y.); libr@usts.edu.cn (B.L.)
* Correspondence: xiaofang@mail.usts.edu.cn; Tel.: +86-0512-68092481

Abstract

Sulfonamide antibiotics (SAs) are frequently detected in aquatic environments worldwide, raising concerns about their environmental impact. Adsorption using biochar is a promising approach, but pristine biochars often exhibit limited removal efficiencies. In this study, biochars derived from spent coffee grounds were prepared under limited oxygen in a muffle furnace (LBC) and CO_2 in a tube furnace (CBC) at 500, 700, and 900 °C, and their adsorption performance toward sulfapyridine (SPY), sulfamerazine (SM1), and sulfamethazine (SM2) was investigated. The results revealed a pronounced temperature-dependent effect. At 500 and 700 °C, LBC exhibited comparable to or better adsorption than CBC. However, at 900 °C, CBC900 had the highest specific surface area (1025 $m^2 \cdot g^{-1}$) and total pore volume (0.5583 $cm^3 \cdot g^{-1}$) among the studied biochars. Under neutral pH and 25 °C, CBC900 exhibited the highest Langmuir-estimated maximum adsorption capacities of 262.7, 220.1, and 244.5 $mg \cdot g^{-1}$ for SPY, SM1, and SM2, respectively. Positive correlations between the estimated adsorption capacities and specific surface area, total pore volume, and micropore volume remained statistically significant after CBC900 was omitted from the analysis. These findings highlight the potential of high-temperature pyrolysis under CO_2 flow to produce spent coffee ground-derived biochar for sulfonamide removal without further modification.

Keywords: biochar; pyrolysis atmosphere; adsorption; sulfonamide antibiotics

1. Introduction

Sulfonamide antibiotics (SAs) are a class of broad-spectrum antibiotics that are widely used because of their effectiveness and relatively low cost [1–4]. SAs can enter the environment through aquaculture discharge, agricultural runoff, and wastewater effluents and have been detected in water and soil [5,6]. Although SAs are often detected at relatively low concentrations [7], studies have reported effects on aquatic organisms, including inhibited algal growth [8], impaired fish development, and morphological abnormalities [9–11]. Chronic low-dose exposure has also been associated with allergic reactions [12], changes in the intestinal microbiota [13], and antibiotic resistance [14–16]. Therefore, the effective removal of SAs from contaminated water is of particular importance.

Methods used to remove SAs include biological treatment, advanced oxidation processes, and adsorption [17]. Adsorption has received attention because it can be effective and relatively simple to operate [18–20]. Carbonaceous materials, including biochar, hydrochar, activated carbon, graphene, and carbon nanotubes, are particularly attractive adsorbents owing to their specific surface areas, pore structures, and surface functional groups [18,19]. Biochar is of particular interest because it can be produced from waste biomass [21–23], typically through pyrolysis under oxygen-limited conditions [24–26]. However, critical reviews

Check for updates

Academic Editor: Biao Song

Received: 3 November 2026
Revised: 21 November 2026
Accepted: 25 November 2026
Published: 27 November 2026

Copyright: © 2026 by the authors. Licensee MDPI, Basel, Switzerland. This article is an open access article distributed under the terms and conditions of the Creative Commons Attribution (CC BY) license.

indicate that although biochar adsorption of antibiotics has been widely reported, the performance of pristine biochars remains highly variable, and the underlying structure–adsorption relationships—particularly those governing SAs—are still insufficiently understood [27,28]. SCG contains lignin, cellulose, and hemicellulose [29]. Previous studies have reported that biochars produced from these biomasses have porous structures, high specific surface area, and thermal stability [30–32]. These properties make SCG a potential feedstock for biochar used in water treatment. Zhang et al. synthesized biochar from spent coffee grounds (SCG) within a temperature range of 200–700 °C, achieving adsorption capacities of 121.5 $\mu g \cdot g^{-1}$ for sulfadiazine and 130.1 $\mu g \cdot g^{-1}$ for sulfamethoxazole [33]. Since then, most SCG-derived adsorbents have relied on chemical modification or activation strategies, such as NaOH activation [34] and metal impregnation [35], which improve adsorption capacity but add reagent cost and the risk of secondary pollution [36]. By contrast, studies that tune the pyrolysis conditions themselves to optimize the structure of SCG biochar remain scarce, and their adsorption performances remain widely scattered [34].

Pyrolysis temperature is an important factor affecting the physicochemical properties of biochar. During thermochemical conversion, biomass components decompose, and oxygen-containing functional groups may form within the 400–500 °C range [37,38]. At higher temperatures, aromatic structures become more condensed, while thermally unstable functional groups tend to decrease, which increases the hydrophobicity of biochar [39]. These transformations can substantially modify the surface area, pore structure, surface chemistry, and adsorption properties of biochar. For example, higher-temperature biochars have been reported to exhibit enhanced surface areas and adsorption capacities for inorganic and organic contaminants compared with their low-temperature counterparts [24,40,41]. For instance, a 700 °C biochar's adsorption for sulfapyridine outperformed lower-temperature counterparts owing to its larger surface area and higher hydrophobicity [42]. However, it is also reported that this improvement is not monotonic. The surface area and adsorption capacity of biochars typically peak at an intermediate temperature and decline at excessively high temperatures owing to ash melting, pore blockage, or structural collapse [42–44], and adsorption capacities tend to level off beyond an optimum temperature [45]. Moreover, the temperature-dependent evolution of biochar is strongly influenced by the precursor composition. For SCG-derived biochar in particular, the structural and adsorption responses to extreme pyrolysis temperatures (e.g., ≥800 °C) remain insufficiently understood. Therefore, identifying the temperature-dependent structural evolution of SCG biochar is essential for optimizing its adsorption performance.

Beyond temperature, the pyrolysis atmosphere can exert a strong influence on the resulting biochar structure and surface chemistry [46–48]. Although conventional biochar production is commonly performed under inert or oxygen-limited conditions, CO_2 can participate in high-temperature gasification through the Boudouard reaction, particularly above approximately 750 °C, thereby promoting carbon etching and pore development [49,50]. In contrast, incorporating trace oxygen can accelerate the decomposition of volatile biomass components and influence carbonization and aromatic structure formation [46,51]. Thus, pyrolysis atmosphere is an active factor governing the structural evolution and surface properties of biochar. Pyrolysis temperature also changes biochar structure, but how atmosphere and temperature jointly affect SCG-derived biochar and its adsorption for SAs remains unclear. In particular, systematic comparisons of SCG biochars prepared under different atmospheres and temperatures are limited, and the implications of these changes for sulfonamide adsorption require further investigation.

In this study, SCG was pyrolyzed under CO_2 in a tube furnace and oxygen-limited conditions in a muffle furnace at 500, 700, and 900 °C. The resulting biochars were characterized in terms of specific surface area, pore structure, surface functional groups, and

hydrophobicity. Sulfapyridine (SPY), sulfamerazine (SM1), and sulfamethazine (SM2) were selected to evaluate adsorption performance. Batch adsorption experiments, physicochemical characterization, and molecular-level calculations were then used to examine how the preparation conditions affected biochar properties and SA adsorption.

2. Materials and Methods

2.1. Materials and Reagents

The SCG was obtained from Arabica coffee beans grown in the Kochere region of Ethiopia. The target SAs, including SPY (≥98%), SM1 (≥99%), and SM2 (≥99%), were obtained from Aladdin Reagent Co., Ltd. (Shanghai, China). Other reagents, including HCl, NaOH, NaCl, $NaHCO_3$, and Na_2SO_4, were of analytical grade. Methanol of high-performance liquid chromatography (HPLC) grade was applied for analytical purposes.

2.2. Preparation of Biochars

2.2.1. Biochar Prepared in a CO_2 Atmosphere (CBC)

The pristine SCG was washed with deionized water and dried at 105 °C for 36 h. Then the samples were ground and passed through a 50-mesh sieve. The pretreated SCG was pyrolyzed in a tube furnace (SK2-4-12DZ, Jinan Jingrui Analytical Instruments Co., Ltd., Jinan, China) with a quartz boat under a CO_2 atmosphere. The crucible was lidded with a slight gap. Before heating, high-purity N_2 (99.999%) was purged through the quartz tube for 30 min to displace air inside the reactor. The N_2 flow rate was maintained at 200 mL min^{-1} throughout pyrolysis and cooling. The samples were heated to 500, 700, and 900 °C at a rate of 5 °C·min^{-1} and held at the target temperature for 2 h [52]. After thermal preservation, the sample was naturally cooled to room temperature inside the tube furnace under continuous N_2 protection. After that, the biochars were ground, passed through a 100-mesh sieve, and labeled as CBC500, CBC700, and CBC900, respectively [53].

2.2.2. Biochar Prepared in an Oxygen-Limited Atmosphere (LBC)

To create an oxygen-limited environment, the pretreated SCG were placed in a fully covered crucible and heated in a muffle furnace (KSL-1100X, Hefei Kejing Material Technology Co., Ltd., Hefei, China) without gas purging [54–56]. Heating rate, pyrolysis temperatures, and residence time were identical to those used for the CBC group. After pyrolysis, the power was turned off, and the crucible remained covered with a lid inside the muffle furnace for natural cooling to room temperature. The obtained biochars were labeled as LBC500, LBC700, and LBC900. Biochar yield was calculated as the mass of dry biochar recovered after pyrolysis divided by the initial mass of dry SCG, expressed as a percentage.

The two systems represent two practical pyrolysis strategies commonly used in biochar research. This comparison cannot decouple the furnace type effect from the atmosphere condition.

2.3. Characterization

Scanning electron microscopy (SEM), specific surface area (SSA) and porosity analysis, water contact angle (WCA), Fourier-transform infrared spectroscopy (FTIR), X-ray photoelectron spectroscopy (XPS), Raman spectroscopy, and zeta-potential measurements were carried out to probe the physicochemical properties of the biochars. Thermogravimetric analysis (TG) of the SCG was also conducted to simulate the pyrolysis process. Ash content was determined gravimetrically and expressed as the mass of residue remaining after combustion as a percentage of the initial dry biochar mass. Detailed instrument infor-

mation and measurement parameters for all characterizations are provided in Text S1 of the Supporting Information.

2.4. Adsorption Experiments

2.4.1. Adsorption Isotherm Experiments

The solutions SPY, SM1, and SM2 were prepared in 0.01 M NaCl to maintain a stable ionic strength and the initial concentrations were set at 0.5, 1, 1.5, 2, 3, 4, 5, 6, 7, 8, 9, and 10 mg·L^{-1}. The solution volume and corresponding biochar dosage were optimized based on preliminary experiments to ensure that the adsorption percentage at equilibrium remained within the range of 30 to 80%. The dosages (solid-to-liquid ratios) used for the different biochars are listed in Table S1. After sealing, the vials were placed in a thermostatic shaker and mixed at 105 rpm and 25 °C for 6 days to ensure complete equilibrium. After that, the liquid phase was sampled using a 0.22 μm PTFE membrane filter. The liquid equilibrium concentration (Ce) of SAs was quantified using HPLC (LC-20AT, Shimadzu, Kyoto, Japan) equipped with an Eclipse XDB C18 chromatographic column (5 μm, 4.6 × 150 mm) and a diode array detector (SPD-M20A, Shimadzu, Japan). The mobile phase was methanol and 0.1% aqueous formic acid (35:65, v/v) at a flow rate of 0.5 mL·min^{-1}. The column temperature was set at 35 °C and the detection wavelengths were at 263, 267, and 265 nm for SPY, SM1, and SM2, respectively. All groups were performed in duplicate, and blank controls without biochar were prepared to account for any non-target losses.

2.4.2. Effects of Solution pH and Coexisting Anions

Since adsorption performance varied considerably among the biochars, a uniform dosage could result in nearly complete removal by CBC900 or negligible removal by less effective biochars, making changes difficult to detect. Therefore, different biochar dosages were used here, with the solid-to-liquid ratios kept consistent with those in the adsorption isotherm experiments (Table S1). The solution pH was adjusted to 1, 3, 5, 7, 9, and 11, and the initial SA concentration was set at 3 mg·L^{-1}. Furthermore, to evaluate the influence of ubiquitous anions (Cl^-, HCO_3^- and SO_4^{2-}) on the adsorption of SAs by LBC900 and CBC900, the removal efficiencies of 5 mg L^{-1} SAs were determined in the presence of these anions at varying concentrations (0, 1, and 10 mg L^{-1}). Each group, including blank groups, was conducted in triplicate.

2.5. Data Processing

To describe the adsorption behavior of SAs onto the biochars, Langmuir and Freundlich models were employed, as mathematically expressed in Equations (1) and (2), respectively:

$$\frac{C_e}{q_e} = \frac{C_e}{q_m} + \frac{1}{q_m K_L} \quad (1)$$

where q_e and C_e represent the equilibrium adsorption capacity (mg·g^{-1}) and residual adsorbate concentration (mg·L^{-1}), respectively; q_m (mg·g^{-1}) corresponds to the theoretical monolayer capacity, while K_L (L·mg^{-1}) reflects the Langmuir affinity coefficient.

$$q_e = K_F C_e^{\frac{1}{n}} \quad (2)$$

where n (dimensionless) reflects the surface heterogeneity of the biochar; K_F [mg · g^{-1}/(mg · L^{-1})$^{1/n}$] is the Freundlich capacity factor associated with adsorption energy.

3. Results and Discussion

3.1. Physicochemical Properties of Biochars

3.1.1. SEM Analysis

SEM observations highlighted that the porous structure of biochars pyrolyzed under distinct conditions underwent different structural evolution as temperature elevated (Figure 1). For CBC samples, the surface became progressively rougher and more porous as the temperature increased, with CBC900 exhibiting a highly developed pore network and abundant wrinkled structures. This is primarily attributed to the Boudouard reaction that occurs at temperatures exceeding 750 °C, which significantly promotes pore propagation via carbon gasification [57]. The enhanced porous structure of CBC900 is expected to increase the accessibility of adsorption sites and facilitate the diffusion of SAs molecules into the carbon framework. In comparison, while the LBC series also shows an increase in porosity with rising temperature, its structural characteristics differ significantly from those of the CBC series. At 500 and 700 °C, LBC exhibits relatively more developed pores than CBC prepared at the same temperature, suggesting that LBC favored initial pore formation during biomass carbonization. However, at 900 °C, LBC900 showed a less pronounced porous structure and a smoother surface morphology compared with CBC900. The limited pore development of CBC may result from the absence of gasification-induced activation, while excessive thermal treatment could promote structural rearrangement and partial pore blockage caused by condensed carbonaceous species. Therefore, the SEM observations suggest that CO_2 activation becomes increasingly important for maintaining and expanding pore structures at elevated temperatures.

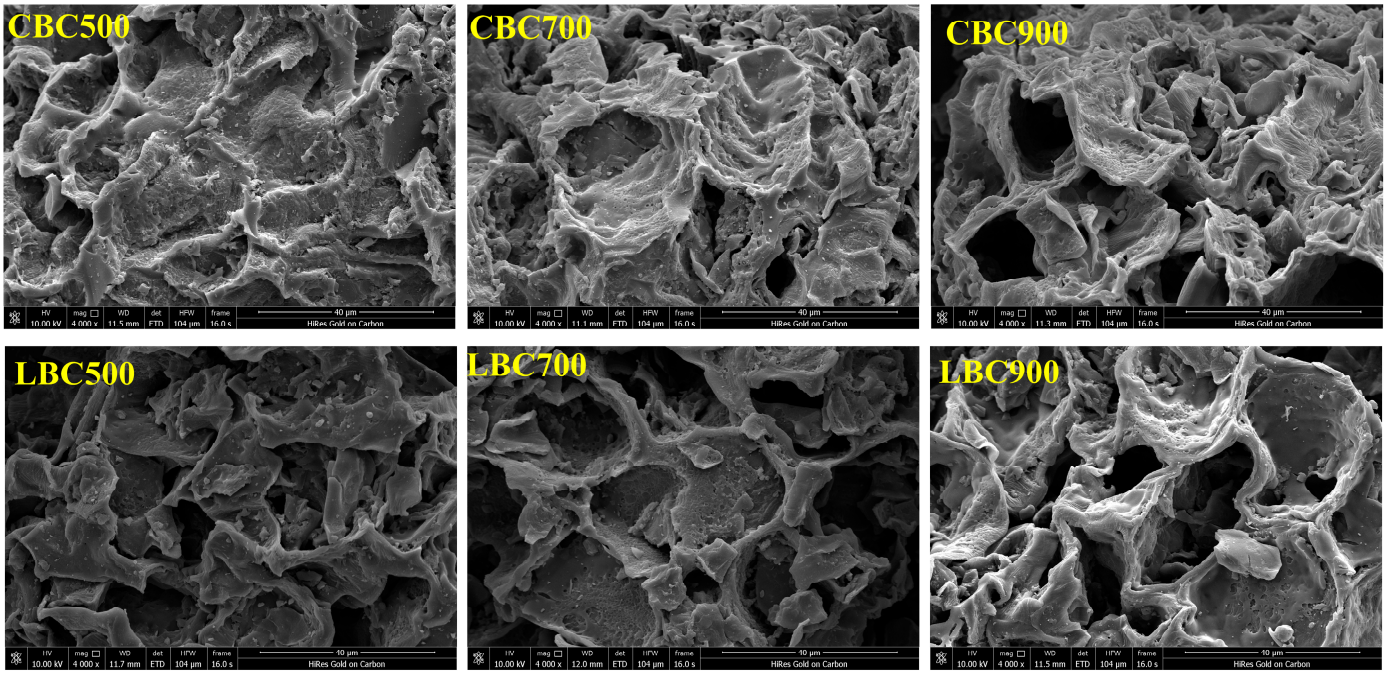


Figure 1. SEM micrographs of biochars prepared under different pyrolysis conditions.

3.1.2. SSA and Pore Volume

The SSA and porosity of biochars were strongly dependent on both pyrolysis temperature and reaction conditions (Table S2). At 500 and 700 °C, LBC exhibited higher SSA and total pore volume (V_{total}) than CBC, suggesting that the LBC condition promoted the initial formation of porous structures during biomass carbonization. However, this trend was reversed at 900 °C. The SSA and V_{total} of CBC900 reached 1025 $m^2 \cdot g^{-1}$ and 0.558 $cm^3 \cdot g^{-1}$,

respectively, which were substantially higher than those of LBC900 (436.4 $m^2 \cdot g^{-1}$ and 0.227 $cm^3 \cdot g^{-1}$). These results demonstrate that the effect of pyrolysis condition on biochar porosity is strongly temperature-dependent. Above approximately 750 °C, CO_2 participates in the Boudouard reaction, consuming carbon atoms and generating additional pores through carbon gasification [58]. To verify this transition, CBC prepared at 800 °C (CBC800) was synthesized as an intermediate-temperature sample. Compared with CBC700, CBC800 exhibited a more than threefold increase in SSA and pore volume, accompanied by a micropore proportion of 93%, indicating rapid micropore development during CO_2 activation. At 900 °C, this activation effect became even more pronounced, resulting in a dramatic expansion of the pore structure in CBC900. In contrast, LBC showed only limited increases in SSA and pore volume over the same temperature range, suggesting that thermal treatment alone was insufficient to induce comparable pore generation without CO_2-mediated gasification.

To verify the role of atmosphere during the pyrolysis process, the TG and derivative TG (DTG) curves of SCG under Ar (to simulate the oxygen-limited environment) and CO_2 were detected (Figure 2a,b) [59]. During the temperature below 750 °C, the weight-loss trends were generally comparable. However, a distinct difference appeared above approximately 750 °C. Under CO_2 conditions, continuous mass loss was observed at elevated temperatures. The DTG profiles further demonstrate the differences in biomass decomposition behavior. Compared with the oxygen-limited atmosphere, CO_2 exhibited lower maximum weight-loss rates during the primary devolatilization stage. The combined TG/DTG results demonstrate that the role of CO_2 is stage-dependent. It has limited influence during the initial pyrolysis stage but becomes an effective activating agent at high temperatures by inducing carbon gasification, which may further produce more SSA and pore volume at high pyrolysis temperature.

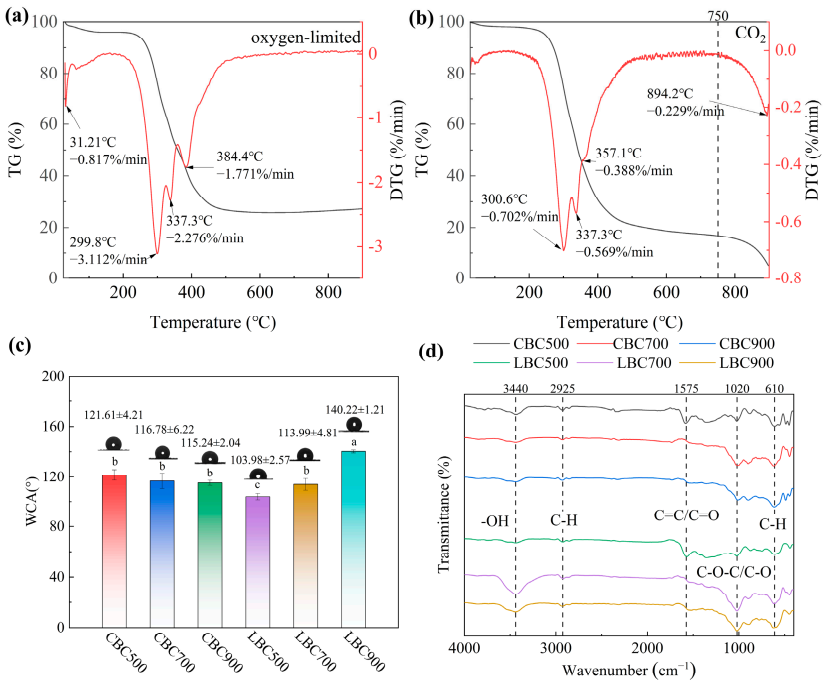


Figure 2. (**a**) Thermogravimetric (TG, black line) and derivative thermogravimetric (DTG, red line) curves of spent coffee grounds under oxygen-limited atmosphere; (**b**) thermogravimetric (TG, black line) and derivative thermogravimetric (DTG, red line) curves of spent coffee grounds under CO_2 atmosphere; (**c**) water contact angle (WCA), with different lowercase letters indicating statistically significant differences ($p < 0.05$); and (**d**) FTIR spectra of biochar.

3.1.3. WCA Analysis

The WCA measurements revealed distinct changes in surface hydrophobicity depending on the pyrolysis conditions (Figure 2c). For CBC, the WCA gradually decreased from 121.6° at 500 °C to 115.2° at 900 °C, indicating a slight reduction in hydrophobicity under the CBC condition with the increased temperature. This transition can be attributed to two factors. First, the CO_2-induced gasification process generates abundant surface defects and pore structures, which can enhance water penetration through capillary effects [60]. Second, carbon gasification preferentially removes relatively reactive carbon domains, resulting in changes in surface elemental composition and a higher relative contribution of oxygen-containing functionalities, thereby increasing surface polarity [50]. In contrast, LBC exhibited an opposite trend, with the WCA increasing from 103.98° (LBC500) to 140.2° (LBC900) as the pyrolysis temperature increased. The enhanced hydrophobicity of LBC at elevated temperatures is mainly associated with the progressive removal of polar oxygen-containing groups during carbonization, accompanied by increased aromatic condensation and surface carbonization. Consequently, the hydrophobicity of LBC900 is significantly higher than that of CBC900. These results demonstrate that pyrolysis conditions strongly regulate the surface hydrophobicity of biochars.

3.1.4. FTIR Analysis

The FTIR spectra of CBC and LBC exhibited similar overall spectral profiles, indicating comparable types of surface functional groups derived from the original biomass (Figure 2d). A broad band around 3440 cm^{-1} corresponding to O–H stretching vibrations was observed in all samples, suggesting the presence of hydroxyl-related functionalities on the biochar surfaces [59,61]. With increasing pyrolysis temperature, the absorption band near 2925 cm^{-1} associated with aliphatic C–H stretching gradually weakened, indicating the progressive decomposition of aliphatic structures during carbonization [59,62]. Meanwhile, the broad band around 1575 cm^{-1}, assigned mainly to aromatic C=C stretching with possible contributions from C=O vibrations, decreased in intensity at higher temperatures [63]. This reduction should not be interpreted simply as the destruction of aromatic structures because the overlapping contribution of oxygen-containing groups, particularly carbonyl species, decreases substantially during thermal treatment [1,63,64]. The structural transformation of the carbon framework will be further discussed based on XPS and Raman analyses. Furthermore, the enhanced intensity of the band near 1020 cm^{-1} in high-temperature CBC may be associated with the preservation or transformation of oxygen-containing ether structures derived from lignin components [59,65,66].

3.1.5. XPS Analysis

XPS survey scans showed pronounced variations in biochar elemental composition across different pyrolysis conditions (Figure 3). Except for CBC900, increasing pyrolysis temperature generally resulted in increased carbon content accompanied by decreased oxygen and nitrogen contents, which is consistent with progressive deoxygenation and denitrogenation during thermal carbonization. In contrast, CBC900 exhibited an apparent decrease in carbon content and a relative enrichment of oxygen and nitrogen compared with CBC700. It can be attributed to carbon consumption induced by the Boudouard reaction, which promotes pore generation and structural rearrangement of the carbon matrix [50]. Consequently, the remaining carbon framework becomes enriched in more condensed structures, although the total carbon content decreases. The apparent increase in O and N contents may result from the relative enrichment of heteroatoms after preferential carbon removal by CO_2 gasification.

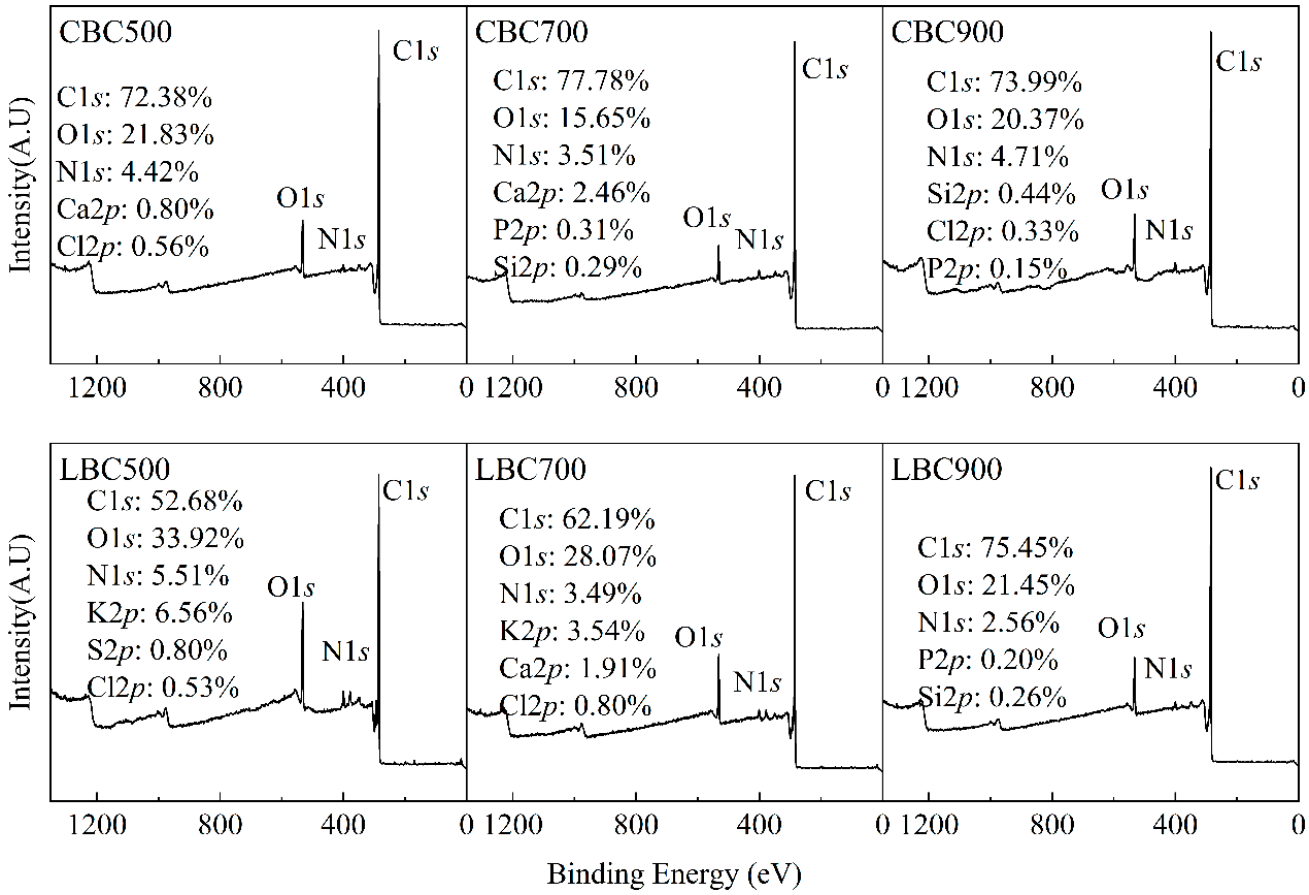


Figure 3. XPS survey spectra of CBC500, CBC700, CBC900, LBC500, LBC700, and LBC900.

The C1*s* spectra further demonstrated the evolution of carbon bonding configurations (Figure S1). For CBC, the proportion of C–C/C=C species increased from 57.7% at 500 °C to 61.53% at 700 °C, followed by a slight decrease to 59.0% at 900 °C (Figure S1). Meanwhile, oxygen-containing carbon species (C–O/C=O) continuously decreased from 41.84% to 29.23%, indicating progressive removal of oxygenated functionalities during thermal treatment [25]. The slight decline in C–C/C=C proportion at 900 °C does not necessarily indicate reduced carbon ordering because CO_2 gasification simultaneously removes carbon from the matrix. Instead, the structural evolution should be considered together with Raman analysis and pore development results. In contrast, the C–C proportion in LBC steadily increased from 64.69% to 73.24% as pyrolysis temperature increased from 500 to 900 °C (Figure S1). The N1*s* spectra show that the proportion of pyridinic nitrogen in both biochars significantly decreased as temperature rose, suggesting its lower thermal stability during carbonization (Figure S2). Meanwhile, pyrrolic N became increasingly enriched, suggesting the rearrangement of nitrogen species within the aromatic carbon framework. The increased proportion of pyrrolic-N may provide additional hydrogen-bonding sites and facilitate specific interactions with SAs molecules. The O1*s* spectra showed that CBC retained a relatively higher proportion of hydroxyl-related oxygen species compared with LBC (Figure S3), indicating that pyrolysis condition affected the distribution of oxygen-containing functionalities on biochar surfaces.

3.1.6. Raman Spectroscopic Analysis

Raman spectroscopy characterized the structural ordering and defect evolution of the biochar carbon skeleton (Figure 4). The D band (~1350 cm^{-1}) corresponds to disordered carbon structures associated with defects, while the G band (~1580 cm^{-1}) represents the

in-plane vibration of sp^2-hybridized carbon domains. The I_D/I_G ratio is commonly used to assess the degree of structural disorder in carbon materials, where a lower value generally indicates increased carbon ordering and aromatic condensation [60,67]. The I_D/I_G ratios of both CBC and LBC decreased progressively with increasing pyrolysis temperature. Specifically, the I_D/I_G value of CBC decreased from 3.970 at 500 °C to 2.604 at 900 °C, while that of LBC decreased from 4.620 to 2.820. This trend indicates that higher pyrolysis temperatures accelerated carbonization, converting amorphous carbon networks into condensed aromatic rings [25]. Under identical pyrolysis temperatures, CBC exhibited slightly lower I_D/I_G values than LBC at 500 and 900 °C, whereas the difference became negligible at 700 °C. These results suggest that the CBC condition may promote carbon structural rearrangement at elevated temperatures.

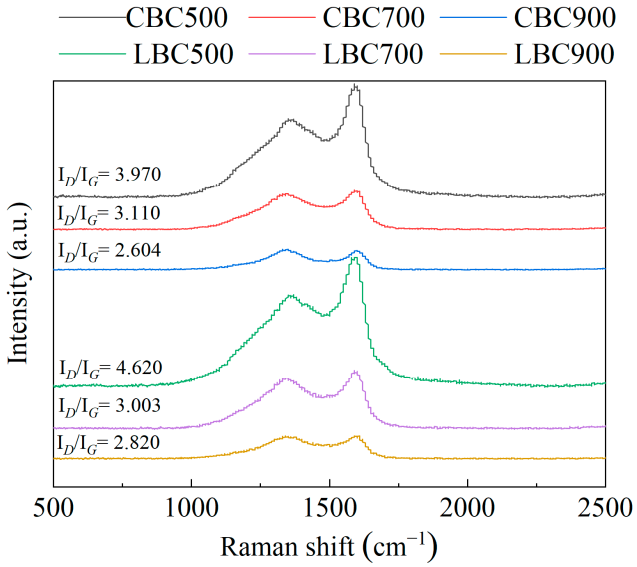


Figure 4. Raman spectra of the biochar samples.

3.1.7. Yield and Ash Content of Biochars

The yield and ash content of the biochars are summarized in Table S3. For both pyrolysis conditions, biochar yield decreased continuously with increasing temperature, reflecting the progressive release of volatile components and carbon conversion during thermal treatment. It should be noted that CBC and LBC were prepared using different reactor systems: CBC was synthesized in a tube furnace with a gapped-lid crucible under continuous gas purging, while LBC was pyrolyzed in a fully covered crucible within a muffle furnace. Variations in furnace configuration and volatile residence time can alter devolatilization behavior and secondary reactions of volatile matter. When the temperature increased from 700 to 900 °C, the yield of CBC decreased from 24.21% to 14.54%, whereas that of LBC decreased only slightly from 24.84% to 21.38%. This significant difference indicates that CO_2 promoted additional carbon consumption at elevated temperatures through gasification reactions, consistent with the enhanced pore development observed in BET analysis. At 500–700 °C, the yield variations in CBC and LBC were relatively comparable, suggesting that biomass devolatilization rather than atmosphere-induced carbon activation dominated the early pyrolysis stage. Therefore, the distinct yield loss of CBC only became evident when the temperature was sufficiently high for CO_2 to participate in carbon gasification.

Opposite to the trend in yield, ash fraction in both biochars rose progressively at higher pyrolysis temperatures. This increase was particularly evident for CBC, where carbon removal by CO_2 gasification resulted in the relative concentration of inorganic mineral

components within the remaining solid phase [50]. To confirm that this increase stems from relative enrichment, the feedstock-normalized ash mass (yield × ash content) was calculated. The values were 0.753 wt%, 0.804 wt% and 0.833 wt% for CBC500, CBC700 and CBC900, respectively. The nearly constant ash mass on a feedstock basis shows that inherent inorganic constituents from raw coffee grounds were largely preserved, and continuous carbon loss concentrated minerals in the residual solid. Ash content alone cannot identify whether these minerals contribute to sulfonamide adsorption. Minerals may affect adsorption via pH variation induced by mineral dissolution or direct surface binding of sulfonamides [68]. Previous studies show mineral effects on sulfonamide adsorption are system-dependent, and isolated ash fractions display limited adsorption capacity [69]. Overall, such findings highlight an inherent compromise between structural development and yield retention: high-temperature CO_2 treatment sacrifices part of the carbon mass but generates a highly porous carbon framework favorable for adsorption applications.

3.2. Adsorption Performance and Mechanisms

3.2.1. Adsorption Isotherms

The adsorption isotherms of SAs on the biochars are presented in Figure 5. For all biochars, the adsorption performance increased continuously along with the elevation of initial SAs concentration and eventually approached a plateau. For biochars prepared under the same atmosphere, the adsorption capacity for a specific SA increased with rising pyrolysis temperature. At 500 °C, CBC and LBC exhibited comparable adsorption performance, suggesting that the difference in preparation atmosphere had a limited influence on adsorption at relatively low temperatures. At 700 °C, LBC showed slightly higher adsorption capacity than CBC, which was consistent with its larger surface area at this temperature (Table S2). However, when the temperature increased to 900 °C, CBC displayed a remarkable enhancement in adsorption capacity and substantially outperformed LBC.

Equilibrium isotherms were fitted via Langmuir and Freundlich models (Table S4). Both models provided acceptable fitting results. The maximum adsorption capacity indicated with Langmuir fitting results by CBC900 were 262.7, 220.1, and 244.5 $mg{\cdot}g^{-1}$ for SPY, SM1, and SM2, respectively, which is much larger than that by LBC900 (33.31, 30.42, and 23.86 $mg{\cdot}g^{-1}$ for SPY, SM1, and SM2, respectively) or that by CBC700 (0.2866, 0.1882, 0.2297 $mg{\cdot}g^{-1}$ for SPY, SM1, and SM2, respectively) (Table S4). The adsorption of SPY and SM2 was better described by the Freundlich model, suggesting heterogeneous adsorption sites and possible multilayer adsorption characteristics. In contrast, SM1 showed a relatively better fit with the Langmuir model, implying a more dominant monolayer adsorption behavior [70,71]. Although the Freundlich model yielded a better fit for most adsorption systems in this study, the Freundlich constant K_F is an empirical parameter coupled with $1/n$ and is not suitable for quantitative comparison of adsorption capacity. Therefore, Langmuir Q_m was adopted for subsequent performance comparison across different biochar samples and literature data. The adsorption performance of the prepared biochar was further compared with previously reported spent coffee grounds or other biochar that had not undergone extra activation, as shown in Table S5. Overall, the CBC900 developed in this work exhibits superior adsorption capacity toward the studied SAs compared with most unactivated spent coffee grounds or other biochars under similar pyrolysis conditions. Notably, this superior performance is maintained even when accounting for the loss of biochar yield at high temperature. The yield of CBC dropped from 24.21% (CBC700) to 14.54% (CBC900), requiring a 1.67-fold increase in carbon-normalized adsorption capacity to match CBC700 on a raw-feedstock basis (Table S3). The measured adsorption capacity of CBC900 far exceeds this critical threshold for all tested SAs, confirming its advantage in raw material utilization.

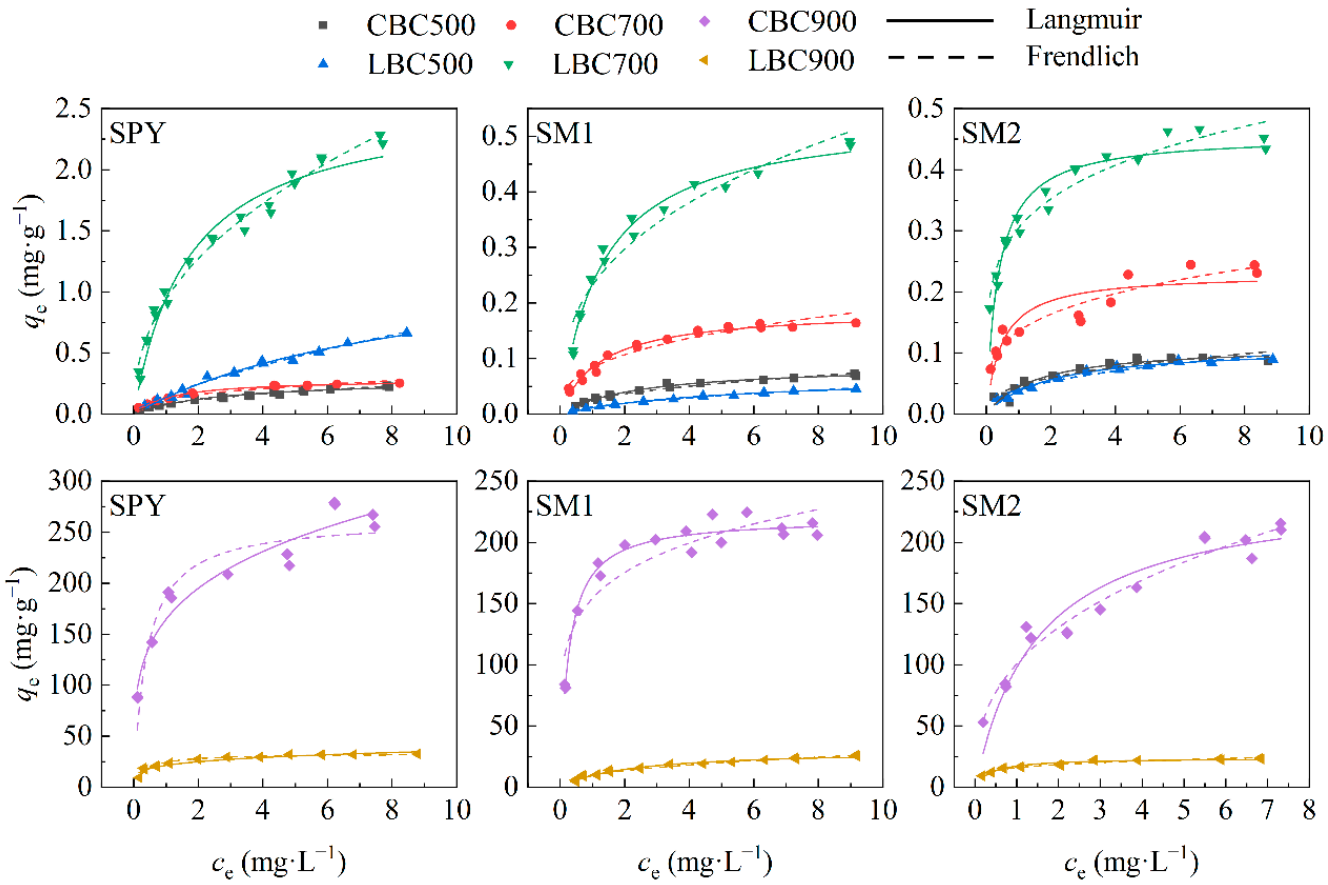


Figure 5. Adsorption isotherms of SAs onto the biochars.

3.2.2. Relationship Between Adsorption and Biochar Properties

The differences in SA adsorption between the two biochar preparation routes varied with pyrolysis temperature (Figure 5). Pearson correlation analysis was applied to explore associations between biochar properties and the Langmuir-estimated maximum adsorption capacity (Q_m) of the three SAs (Figure 6). In the full dataset, Q_m was positively correlated with SSA, total pore volume, micropore volume, medium-large pore volume, and pyrrolic N content ($p < 0.05$). The correlations between I_D/I_G ratio and Q_m were weakly negative and statistically non-significant. The correlations of I_D/I_G ratio with SSA and pore volume were negative and statistically non-significant. A non-significant negative correlation between I_D/I_G ratio and SSA or pore volume was observed, as well as a non-significant positive correlation between pyrrolic-N and SSA, total pore volume, or micropore volume. However, a significant correlation between medium-large pore volume and pyrrolic-N content was observed ($p < 0.05$).

To assess the influence of CBC900, the Pearson correlation coefficients were recalculated after omitting this sample (Figure S4 and Table S6). After CBC900 was omitted, the positive correlations of Q_m with SSA, total pore volume and micropore volume remained statistically significant, whereas those with medium-large pore volume no longer reached statistical significance for SM1 or SM2. The correlations with pyrrolic N content and Q_m changed from statistically significant positive values to non-significant negative values. Thus, the positive associations observed in the full dataset were sensitive to the inclusion of CBC900. Previous studies have proposed that π–π interactions between aromatic carbon domains and the aromatic rings of sulfonamides may contribute to adsorption [72,73]. In this study, the weak negative correlations between I_D/I_G ratio and Q_m changed little after CBC900 was

omitted and did not reach statistical significance in either analysis. These correlations alone are insufficient to assess the contribution of π–π stacking.

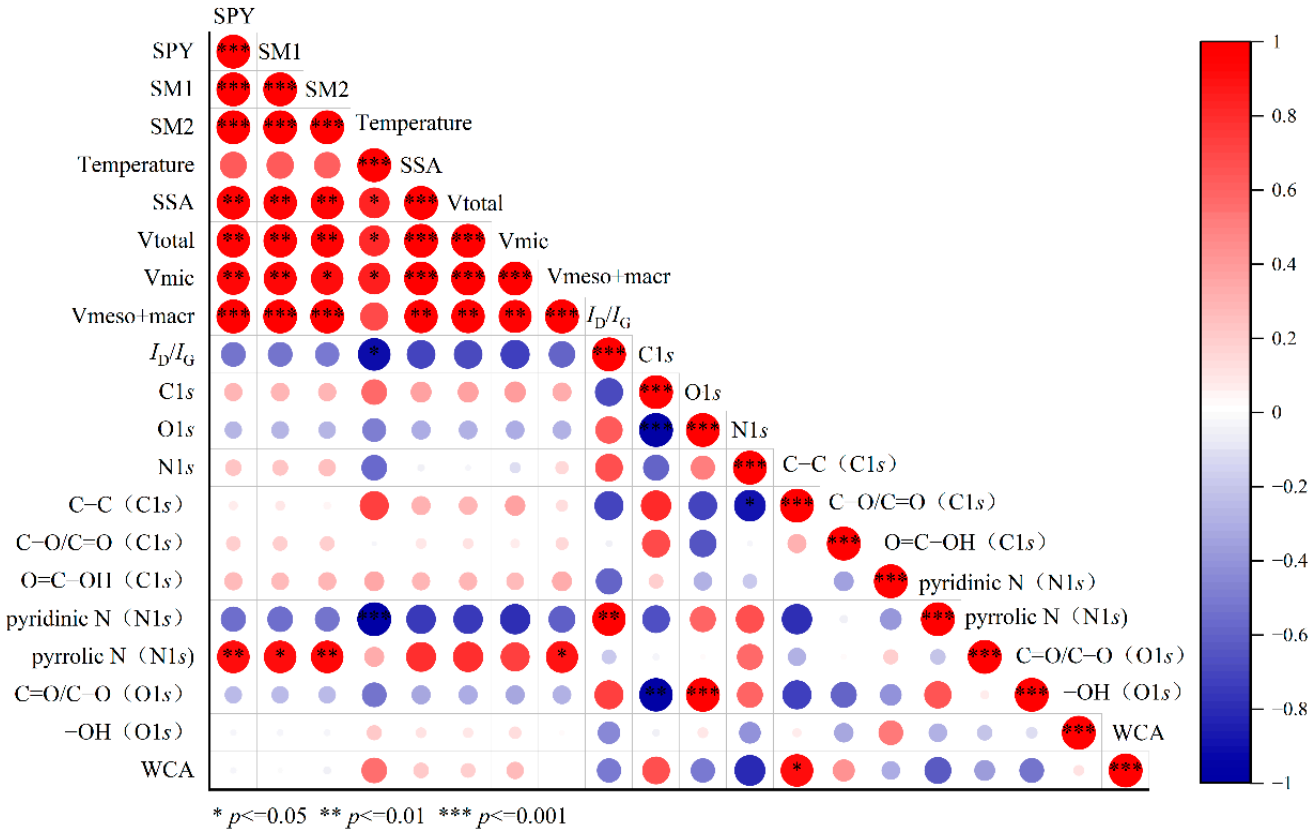


Figure 6. Pearson correlation heatmap between the Langmuir maximum adsorption capacity (Q_m) of SAs and the physicochemical properties and pyrolysis temperatures of biochars.

From CBC700 to CBC900, SSA and pore volume increased by approximately 13-fold (Table S2), whereas the Langmuir-estimated Q_m values increased by more than three orders of magnitude (Table S4). The larger SSA and more developed pore structure of CBC900 may have contributed to its higher SA uptake. The association between micropore volume and Q_m in both analyses is consistent with a possible role for micropore filling. When pore widths are comparable to the dimensions of the adsorbate molecules, adsorption potentials from opposing pore walls can overlap and favor adsorption [74,75].

Nitrogen-containing sites on carbon surfaces have been proposed as potential participants in hydrogen bonding with organic adsorbates [76]. To explore how SAs might bind to nitrogen-containing sites, DFT calculations were applied to compare the adsorption energies and optimized geometries of SAs on carbon models containing pyrrolic or pyridinic N (Figures S5–S7). The calculation method is listed in Text S2. The electrostatic potential maps identified electron-rich sulfonyl oxygen atoms and regions of positive potential around certain hydrogen atoms as potential sites for intermolecular interactions (Figure S5). In the SA–H orientation, all three SAs exhibited more negative calculated adsorption energies on the pyridinic N model than on the pyrrolic N model. Among the configurations examined, the lowest-energy structures for SM1 and SM2 were obtained on the pyrrolic N model in the SA–O orientation, whereas SPY favored the pyridinic N model in the SA–H orientation (Figure S7). In the SA–O configurations, hydrogen bonding between the pyrrolic N–H group and a sulfonyl oxygen atom may contribute to the favorable binding of SM1 and SM2. These calculations suggest that the preferred binding site and orientation varied among the three SAs in the model systems.

3.2.3. Influence of Antibiotic Physicochemical Properties on Adsorption

Besides biochar properties, the physicochemical characteristics of SAs molecules also influenced their adsorption behavior. For most biochars, the Langmuir-estimated Q_m followed the order of SPY > SM2 > SM1. For LBC700 and LBC900, the order was SPY > SM1 > SM2 (Table S4). The predominant order was consistent with the ranking of the compounds by logK_{ow} values (Table S7), suggesting that molecular hydrophobicity may partly explain the differences in uptake. The reversal of the SM1 and SM2 order on LBC700 and LBC900 indicates that their relative uptake also depended on the biochar. Differences in heterocyclic structure may influence how the sulfonamides access narrow pores. SPY contains an unsubstituted pyridine ring, whereas SM1 and SM2 contain methyl-substituted pyrimidine rings. These structural differences may affect how the molecules orient at pore entrances and enter narrow micropores [36,77]. Previous studies have also reported that differences in molecular properties can affect sulfonamide adsorption [78]. For SM1, the estimated Q_m was substantially higher on CBC900 than on LBC900, although CBC900 had a lower water contact angle (Figure 2c). The larger SSA and more developed pore structure of CBC900 may have contributed to this difference. Together, these results suggest that molecular properties help explain the uptake order within a given biochar, while differences in biochar properties can alter both the magnitude and the order of uptake.

3.3. Effects of Solution pH and Coexisting Ions on Adsorption Performance

As the adsorption capacity difference in various biochars is substantial, to better compare the influence of solution pH on the adsorption performance, the mass of the biochar applied here for CBC900 and LBC900 is different from other biochars. The adsorption performance of biochars was strongly influenced by solution pH (Figure 7), with relatively lower adsorption under strongly acidic (pH 1) and alkaline conditions (pH 11) [79]. Zeta potential analysis showed that biochar surfaces became positively charged at pH 1 and negatively charged under alkaline conditions (Figure S8). Meanwhile, the ionization state of SAs also varies under different pH environments (Table S7). Under strongly acidic conditions, protonated SA species and positively charged biochar surfaces generated electrostatic repulsion, thereby reducing adsorption efficiency. Conversely, under alkaline conditions, deprotonated SA species and negatively charged biochar surfaces also caused electrostatic repulsion, resulting in suppressed adsorption. Most biochars exhibited optimal adsorption performance around mildly acidic conditions (pH 3), where SAs mainly existed in less charged forms and electrostatic interference was minimized [80]. In addition, partial dissolution of mineral components under acidic conditions may expose additional adsorption sites, although this effect is expected to be secondary compared with pore structure and surface interactions [81,82]. Notably, CBC900 maintained relatively stable adsorption performance over a wider pH range, indicating enhanced tolerance toward changes in solution chemistry.

The effects of coexisting anions on SA adsorption were further evaluated to assess the environmental stability of the two biochars (LBC900 and CBC900) with relative high adsorption performance (Figure 8). At relatively low anion concentrations (1 mg·L^{-1}), negligible changes were observed, indicating limited interference under dilute ionic conditions. When the concentration increased to 10 mg·L^{-1}, certain anions influenced SA adsorption, particularly for LBC900. The adsorption variation may be associated with competition between dissolved anions and SA molecules for surface interaction sites, as well as modification of the interfacial electrostatic environment. In contrast, CBC900 maintained relatively stable adsorption performance regardless of anion type and concentration. The enhanced ionic tolerance of CBC900 can be attributed to its highly developed microporous structure and abundant adsorption sites, which reduce the sensitivity of adsorption performance to

external ionic fluctuations. These findings suggest that CO_2-activated biochar possesses improved stability under complex aqueous conditions.

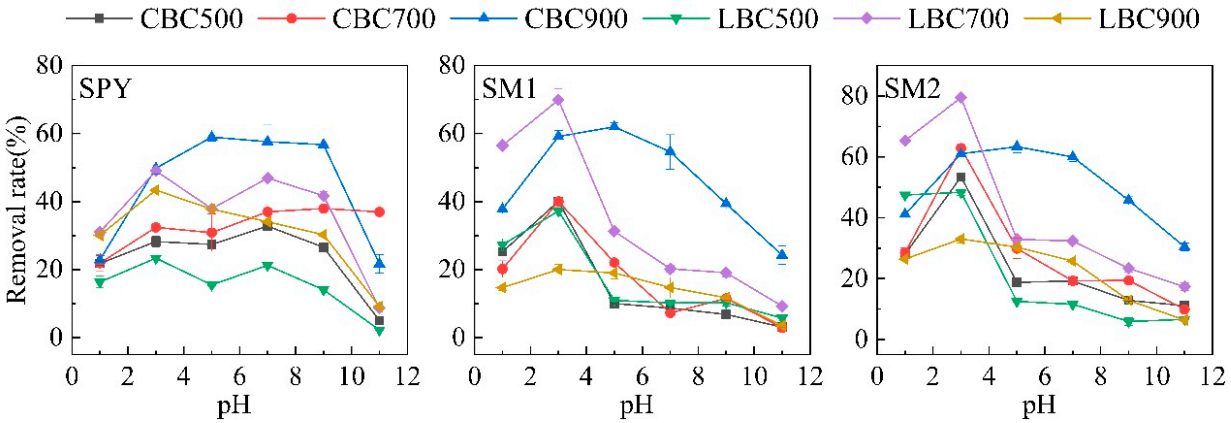


Figure 7. Effects of initial solution pH on the adsorption of SAs by biochars.

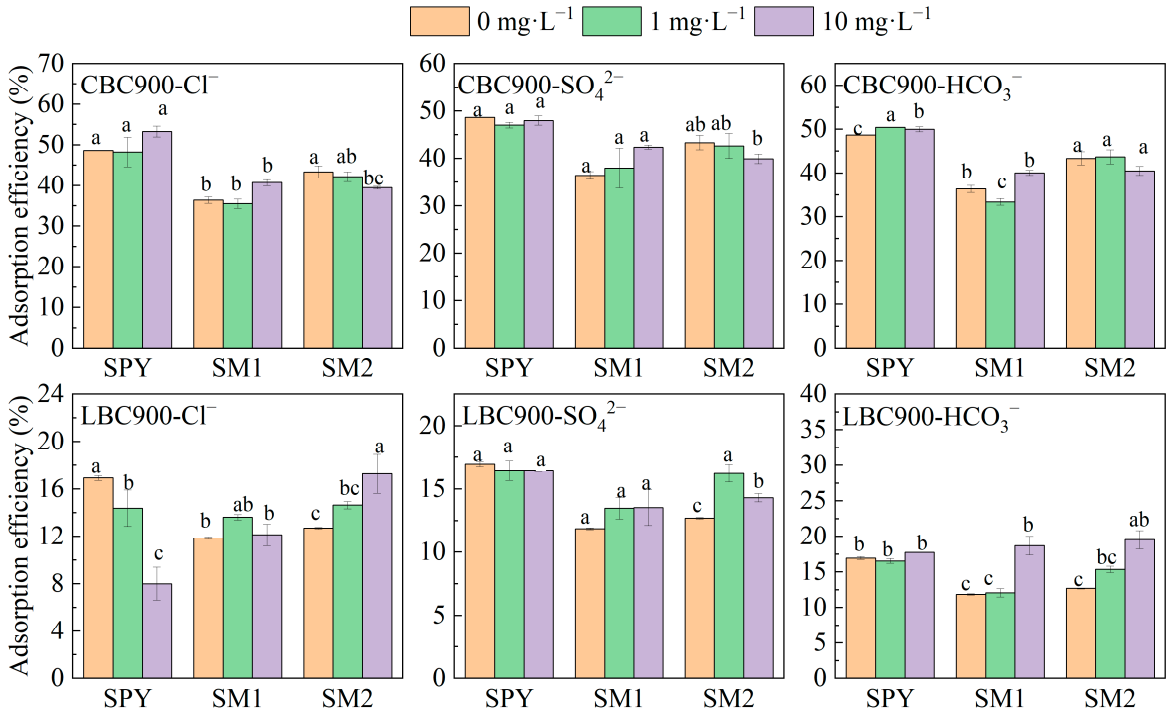


Figure 8. Influence of ionic concentrations on the adsorption of SAs by biochars, with different lowercase letters indicating statistically significant differences ($p < 0.05$).

4. Conclusions

This study compared the physicochemical properties and SA adsorption performance of SCG-derived biochars prepared at 500, 700, and 900 °C in a muffle furnace without external gas purging (LBC) or under continuous CO_2 flow in a tube furnace (CBC). At 500 and 700 °C, LBC favored the development of accessible pore structures and preservation of oxygen-containing functional groups, resulting in slightly higher adsorption performance than CBC. However, at 900 °C, CBC900 achieved the maximum adsorption capacities of 262.7 mg g^{-1} for SPY, 220.1 mg g^{-1} for SM1, and 244.5 mg g^{-1} for SM2, all superior to those of LBC900. CBC900 had the highest SSA (1025 m^2 g^{-1}) and total pore volume (0.5583 cm^3 g^{-1}) among the tested biochars. The positive correlations of adsorption capacity with SSA, total

pore volume, and micropore volume remained statistically significant after CBC900 was excluded from the correlation analysis. Furthermore, CBC900 exhibited improved resistance toward variations in solution pH and coexisting ions, indicating its potential for application in SA removal under varying aqueous environments. Overall, this study demonstrates that high-temperature continuous gas-flow pyrolysis provides an effective strategy for tailoring biochar structures and improving antibiotic adsorption performance. Nevertheless, elevated pyrolysis temperature inevitably brings concerns including increased energy consumption and reduced biochar yield. Future studies should focus on optimizing preparation conditions to balance carbon yield, energy consumption, and adsorption efficiency for sustainable water treatment applications.

Supplementary Materials: The following supporting information can be downloaded at https://www.mdpi.com/article/10.3390/separations13120354/s1, Text S1: Detailed instrument information and measurement parameters for characterizations; Text S2: Method of Density functional theory calculations; Figure S1: High-resolution C1s spectra of biochar; Figure S2: High-resolution N1s spectra of biochar; Figure S3: High-resolution O1s spectra of biochar; Figure S4: Correlation heatmap of biochar properties and SA adsorption capacity after excluding CBC900; Figure S5: Electrostatic potentials of sulfapyridine, sulfamethazine, and sulfadimethoxine; Figure S6: Electrostatic potential of simulated biochar within pyridinic N and pyrrolic N; Figure S7: Adsorption of SAs by simulated biochar within pyridinic N and pyrrolic N; Figure S8: Zeta potentials of the raw biochars; Table S1: Solid-to-liquid ratios applied in adsorption experiment; Table S2: Specific surface area and pore structure parameters of the biochars; Table S3: Yields and ash contents of the biochar samples; Table S4: Fitting parameters of adsorption isotherms for SAs onto the biochars; Table S5: Adsorption performance comparison of raw biochars toward organic pollutants; Table S6: Pearson correlation coefficients (r) and p-values between key physicochemical parameters and Langmuir maximum adsorption capacity (Q_m) of SPY, SM1 and SM2; Table S7: Physicochemical properties of the three SAs. References [29,60,68,83–97] are cited in the Supplementary Materials.

Author Contributions: Conceptualization, W.L. and X.Y.; methodology, W.L. and X.Y.; software, W.L. and B.L.; validation, W.L. and X.S.; formal analysis, X.S.; investigation, W.L. and X.Y.; resources, W.L. and X.Y.; data curation, W.L. and X.Y.; writing—original draft preparation, W.L.; writing—review and editing, B.L. and X.S.; visualization, W.L.; supervision, B.L. and X.S.; project administration, X.S.; funding acquisition, X.S. All authors have read and agreed to the published version of the manuscript.

Funding: This research was funded by the National Natural Science Foundation of China, grant number 41701545.

Data Availability Statement: The raw data supporting the conclusions of this article will be made available by the authors on request.

Acknowledgments: During the preparation of this manuscript, the authors used Gemini 3 Pro for the purposes of visual presentation of the Graphical Abstract. The authors have reviewed and edited the output and take full responsibility for the content of this publication.

Conflicts of Interest: The authors declare no conflicts of interest.

Abbreviations

The following abbreviations are used in this manuscript:

SAs	Sulfonamide antibiotics
SPY	Sulfapyridine
SM1	Sulfamerazine
SM2	Sulfamethazine
LBC	Biochars prepared in an oxygen-limited atmosphere
LBC500	Biochars prepared in an oxygen-limited atmosphere at 500 °C
LBC700	Biochars prepared in an oxygen-limited atmosphere at 700 °C
LBC900	Biochars prepared in an oxygen-limited atmosphere at 900 °C

CBC	Biochars prepared in a CO_2 atmosphere
CBC500	Biochars prepared in a CO_2 atmosphere at 500 °C
CBC700	Biochars prepared in a CO_2 atmosphere at 700 °C
CBC800	Biochars prepared in a CO_2 atmosphere at 800 °C
CBC900	Biochars prepared in a CO_2 atmosphere at 900 °C
SCG	Spent coffee grounds
SEM	Scanning electron microscopy
SSA	Specific surface area
WCA	Water contact angle
FTIR	Fourier-transform infrared spectroscopy
XPS	X ray photoelectron spectroscopy
TG	Thermogravimetric
DTG	Derivative thermogravimetric
HPLC	High-performance liquid chromatography

References

1. Peng, T.; Song, B.; Wang, Y.; Yuan, J.; Yang, Z.; Tang, L. Trophic transfer of sulfonamide antibiotics in aquatic food chains: A comprehensive review with a focus on environmental health risks. *Environ. Pollut.* **2025**, *369*, 125823. [CrossRef] [PubMed]
2. Mai, Z.; Xiong, X.; Hu, H.; Jia, J.; Wu, C.; Wang, G. Occurrence, distribution, and ecological risks of antibiotics in Honghu Lake and surrounding aquaculture ponds, China. *Environ. Sci. Pollut. Res.* **2023**, *30*, 50732–50742. [CrossRef] [PubMed]
3. Zhou, L.; Li, S.; Li, F. Damage and elimination of soil and water antibiotic and heavy metal pollution caused by livestock husbandry. *Environ. Res.* **2022**, *215*, 114188. [CrossRef] [PubMed]
4. Lewis, K. The Science of Antibiotic Discovery. *Cell* **2020**, *181*, 29–45. [CrossRef] [PubMed]
5. Baran, W.; Adamek, E.; Ziemiańska, J.; Sobczak, A. Effects of the presence of sulfonamides in the environment and their influence on human health. *J. Hazard. Mater.* **2011**, *196*, 1–15. [CrossRef] [PubMed]
6. He, Y.; Wang, S.; Li, H.; Han, Z.; Liu, X.; Meng, Q.; Li, J. Adsorption of sulfonamide antibiotics by phosphoric acid-activated passion fruit peel biochar and its plasma regeneration. *J. Water Process Eng.* **2026**, *91*, 110570. [CrossRef]
7. Yi, C.; Shang, J.; Shen, Z.; Sun, Y.; Yang, Y.; Zheng, X.; Peng, Z.; Chen, J.; Liu, Y.; Guo, R.; et al. Distribution and risk characteristics of antibiotics in China surface water from 2013 to 2024. *Chemosphere* **2025**, *375*, 144197. [CrossRef] [PubMed]
8. Białk-Bielińska, A.; Caban, M.; Pieczyńska, A.; Stepnowski, P.; Stolte, S. Mixture toxicity of six sulfonamides and their two transformation products to green algae Scenedesmus vacuolatus and duckweed Lemna minor. *Chemosphere* **2017**, *173*, 542–550. [CrossRef] [PubMed]
9. Yan, Z.; Yang, Q.; Jiang, W.; Lu, J.; Xiang, Z.; Guo, R.; Chen, J. Integrated toxic evaluation of sulfamethazine on zebrafish: Including two lifespan stages (embryo-larval and adult) and three exposure periods (exposure, post-exposure and re-exposure). *Chemosphere* **2018**, *195*, 784–792. [CrossRef] [PubMed]
10. Limbu, S.M.; Zhou, L.; Sun, S.-X.; Zhang, M.-L.; Du, Z.-Y. Chronic exposure to low environmental concentrations and legal aquaculture doses of antibiotics cause systemic adverse effects in Nile tilapia and provoke differential human health risk. *Environ. Int.* **2018**, *115*, 205–219. [CrossRef] [PubMed]
11. Lin, T.; Yu, S.; Chen, Y.; Chen, W. Integrated biomarker responses in zebrafish exposed to sulfonamides. *Environ. Toxicol. Pharmacol.* **2014**, *38*, 444–452. [CrossRef] [PubMed]
12. Ribeiro, C.F.A.; Silveira, G.G.D.O.S.; Cândido, E.D.S.; Cardoso, M.H.; Espínola Carvalho, C.M.; Franco, O.L. Effects of Antibiotic Treatment on Gut Microbiota and How to Overcome Its Negative Impacts on Human Health. *ACS Infect. Dis.* **2020**, *6*, 2544–2559. [CrossRef] [PubMed]
13. Zhang, C.; Chen, Y.; Chen, S.; Guan, X.; Zhong, Y.; Yang, Q. Occurrence, risk assessment, and in vitro and in vivo toxicity of antibiotics in surface water in China. *Ecotoxicol. Environ. Saf.* **2023**, *255*, 114817. [CrossRef] [PubMed]
14. Kim, H.; Kim, J.; Kim, M.; Hyun, S.; Moon, D.H. Sorption of sulfathiazole in the soil treated with giant Miscanthus-derived biochar: Effect of biochar pyrolysis temperature, soil pH, and aging period. *Environ. Sci. Pollut. Res.* **2017**, *25*, 25681–25689. [CrossRef] [PubMed]
15. Zimmermann, P.; Curtis, N. The effect of antibiotics on the composition of the intestinal microbiota—A systematic review. *J. Infect.* **2019**, *79*, 471–489. [CrossRef] [PubMed]
16. Zhang, J.; Zhang, X.; Hu, T.; Xu, X.; Zhao, D.; Wang, X.; Li, L.; Yuan, X.; Song, C.; Zhao, S. Polycyclic aromatic hydrocarbons (PAHs) and antibiotics in oil-contaminated aquaculture areas: Bioaccumulation, influencing factors, and human health risks. *J. Hazard. Mater.* **2022**, *437*, 129365. [CrossRef] [PubMed]
17. Zhao, Y.; He, J.; Pang, H.; Li, L.; Cui, X.; Liu, Y.; Jiang, W.; Liu, X. Anaerobic digestion and biochar/hydrochar enhancement of antibiotic-containing wastewater: Current situation, mechanism and future prospects. *Environ. Res.* **2025**, *264*, 120087. [CrossRef] [PubMed]

18. Yu, F.; Li, Y.; Han, S.; Ma, J. Adsorptive removal of antibiotics from aqueous solution using carbon materials. *Chemosphere* **2016**, *153*, 365–385. [CrossRef] [PubMed]
19. Xiang, Y.; Xu, Z.; Wei, Y.; Zhou, Y.; Yang, X.; Yang, Y.; Yang, J.; Zhang, J.; Luo, L.; Zhou, Z. Carbon-based materials as adsorbent for antibiotics removal: Mechanisms and influencing factors. *J. Environ. Manag.* **2019**, *237*, 128–138. [CrossRef] [PubMed]
20. Ahmed, I.; Lee, H.J.; Jhung, S.H. Covalent-organic polymer-derived carbons: An effective adsorbent to remove sulfonamide antibiotics from water. *Chem. Eng. J.* **2022**, *437*, 135386. [CrossRef]
21. Krasucka, P.; Pan, B.; Ok, Y.S.; Mohan, D.; Sarkar, B.; Oleszczuk, P. Engineered biochar—A sustainable solution for the removal of antibiotics from water. *Chem. Eng. J.* **2021**, *405*, 126926. [CrossRef]
22. Ahmad, M.; Rajapaksha, A.U.; Lim, J.E.; Zhang, M.; Bolan, N.; Mohan, D.; Vithanage, M.; Lee, S.S.; Ok, Y.S. Biochar as a sorbent for contaminant management in soil and water: A review. *Chemosphere* **2014**, *99*, 19–33. [CrossRef] [PubMed]
23. Xue, Y.; Gao, B.; Yao, Y.; Inyang, M.; Zhang, M.; Zimmerman, A.R.; Ro, K.S. Hydrogen peroxide modification enhances the ability of biochar (hydrochar) produced from hydrothermal carbonization of peanut hull to remove aqueous heavy metals: Batch and column tests. *Chem. Eng. J.* **2012**, *200–202*, 673–680. [CrossRef]
24. Zhang, J.B.; Dai, C.; Wang, Z.; You, X.; Duan, Y.; Lai, X.; Fu, R.; Zhang, Y.; Maimaitijiang, M.; Leong, K.H.; et al. Resource utilization of rice straw to prepare biochar as peroxymonosulfate activator for naphthalene removal: Performances, mechanisms, environmental impact and applicability in groundwater. *Water Res.* **2023**, *244*, 120555. [CrossRef] [PubMed]
25. Pei, S.; Zhao, Y.; Li, W.; Qu, C.; Ren, Y.; Yang, Y.; Liu, J.; Wu, C. Critical impact of pyrolysis temperatures on biochars for peroxymonosulfate activation: Structural characteristics, degradation performance and mechanism. *Chem. Eng. J.* **2023**, *477*, 147274. [CrossRef]
26. Grimm, A.; dos Reis, G.S.; Khokarale, S.G.; Ekman, S.; Lima, E.C.; Xiong, S.; Hultberg, M. Shiitake spent mushroom substrate as a sustainable feedstock for developing highly efficient nitrogen-doped biochars for treatment of dye-contaminated water. *J. Water Process Eng.* **2023**, *56*, 104435. [CrossRef]
27. Jia, Y.; Ou, Y.; Khanal, S.K.; Sun, L.; Shu, W.-S.; Lu, H. Biochar-based strategies for antibiotics removal: Mechanisms, factors, and application. *ACS ES&T Eng.* **2024**, *4*, 1256–1274. [CrossRef]
28. Sen, U.; Esteves, B.; Aguiar, T.; Pereira, H. Removal of antibiotics by biochars: A critical review. *Appl. Sci.* **2023**, *13*, 11963. [CrossRef]
29. Zhang, X.; Zhang, Y.; Ngo, H.H.; Guo, W.; Wen, H.; Zhang, D.; Li, C.; Qi, L. Characterization and sulfonamide antibiotics adsorption capacity of spent coffee grounds based biochar and hydrochar. *Sci. Total Environ.* **2020**, *716*, 137015. [CrossRef] [PubMed]
30. Jiang, C.; Bo, J.; Xiao, X.; Zhang, S.; Wang, Z.; Yan, G.; Wu, Y.; Wong, C.; He, H. Converting waste lignin into nano-biochar as a renewable substitute of carbon black for reinforcing styrene-butadiene rubber. *Waste Manag.* **2020**, *102*, 732–742. [CrossRef] [PubMed]
31. Lonappan, L.; Rouissi, T.; Brar, S.K.; Verma, M.; Surampalli, R.Y. An insight into the adsorption of diclofenac on different biochars: Mechanisms, surface chemistry, and thermodynamics. *Bioresour. Technol.* **2018**, *249*, 386–394. [CrossRef] [PubMed]
32. Lobos, M.L.N.; Sieben, J.M.; Comignani, V.; Duarte, M.; Volpe, M.A.; Moyano, E.L. Biochar from pyrolysis of cellulose: An alternative catalyst support for the electro-oxidation of methanol. *Int. J. Hydrogen Energy* **2016**, *41*, 10695–10706. [CrossRef]
33. Zhang, X.; Wang, Y.; Cai, J.; Wilson, K.; Lee, A.F. Bio/hydrochar sorbents for environmental remediation. *Energy Environ. Mater.* **2020**, *3*, 453–468. [CrossRef]
34. Madikizela, L.M.; Pakade, V.E. Trends in removal of pharmaceuticals in contaminated water using waste coffee and tea-based materials with their derivatives. *Water Environ. Res.* **2023**, *95*, e10857. [CrossRef] [PubMed]
35. El-Shafie, A.S.; Mahmoud, R.; Ahsan, I.; Hamdi, H.; Shibl, M.F.; El-Azazy, M. Removal of antibiotics from aqueous solutions: Insights of competitive adsorption onto Ni-impregnated biochar of spent coffee grounds. *Appl. Water Sci.* **2024**, *14*, 209. [CrossRef]
36. Wang, J.; Hou, Y.; Li, X.; Zhao, R.; Mu, X.; Liu, Y.; Huang, C.; Fu, F.; Yang, F. Research progress and prospects of modified biochar in the adsorption and degradation of sulfonamide antibiotics. *Antibiotics* **2026**, *15*, 268, Correction in *Antibiotics* **2026**, *15*, 803. [CrossRef] [PubMed]
37. Fawzy, S.; Osman, A.I.; Mehta, N.; Moran, D.; Al-Muhtaseb, A.H.; Rooney, D.W. Atmospheric carbon removal via industrial biochar systems: A techno-economic-environmental study. *J. Clean. Prod.* **2022**, *371*, 133660. [CrossRef]
38. Wang, D.; Jiang, P.; Zhang, H.; Yuan, W. Biochar production and applications in agro and forestry systems: A review. *Sci. Total Environ.* **2020**, *723*, 137775. [CrossRef] [PubMed]
39. Zheng, X.; Zhou, Y.; Liu, X.; Fu, X.; Peng, H.; Lv, S. Enhanced adsorption capacity of MgO/N-doped active carbon derived from sugarcane bagasse. *Bioresour. Technol.* **2020**, *297*, 122413. [CrossRef] [PubMed]
40. Yu, O.Y.; Harper, M.; Hoepfl, M.; Domermuth, D. Characterization of biochar and its effects on the water holding capacity of loamy sand soil: Comparison of hemlock biochar and switchblade grass biochar characteristics. *Environ. Prog. Sustain. Energy* **2017**, *36*, 1474–1479. [CrossRef]

41. Ke, Y.; Cui, S.; Fu, Q.; Hough, R.; Zhang, Z.; Li, Y.-F. Effects of pyrolysis temperature and aging treatment on the adsorption of Cd^{2+} and Zn^{2+} by coffee grounds biochar. *Chemosphere* **2022**, *296*, 134051. [CrossRef] [PubMed]
42. Ndoun, M.C.; Elliott, H.A.; Preisendanz, H.E.; Williams, C.F.; Knopf, A.; Watson, J.E. Adsorption of pharmaceuticals from aqueous solutions using biochar derived from cotton gin waste and guayule bagasse. *Biochar* **2020**, *3*, 89–104. [CrossRef]
43. Mašek, O.; Buss, W.; Wang, L.; Sun, J.; Wang, X.; Wang, Y.; Skreiberg, Ø. Biochar production under different atmospheres: An overview. *Biochar* **2026**, *8*, 129. [CrossRef] [PubMed]
44. Li, Y.; Xing, B.; Ding, Y.; Han, X.; Wang, S. A critical review of the production and advanced utilization of biochar via selective pyrolysis of lignocellulosic biomass. *Bioresour. Technol.* **2020**, *312*, 123614. [CrossRef] [PubMed]
45. Luo, Q.; Deng, Y.; Li, Y.; He, Q.; Wu, H.; Fang, X. Effects of pyrolysis temperatures on the structural properties of straw biochar and its adsorption of tris-(1-chloro-2-propyl) phosphate. *Sci. Rep.* **2024**, *14*, 25711. [CrossRef] [PubMed]
46. Luo, L.; Xu, C.; Chen, Z.; Zhang, S. Properties of biomass-derived biochars: Combined effects of operating conditions and biomass types. *Bioresour. Technol.* **2015**, *192*, 83–89. [CrossRef] [PubMed]
47. Igalavithana, A.D.; Kim, K.-H.; Jung, J.-M.; Heo, H.-S.; Kwon, E.E.; Tack, F.M.G.; Tsang, D.C.; Jeon, Y.J.; Ok, Y.S. Effect of biochars pyrolyzed in N_2 and CO_2, and feedstock on microbial community in metal(loid)s contaminated soils. *Environ. Int.* **2019**, *126*, 791–801. [CrossRef] [PubMed]
48. Wang, Z.; Ma, X.; Yao, Z.; Yu, Q.; Wang, Z.; Lin, Y. Study of the pyrolysis of municipal sludge in N_2/CO_2 atmosphere. *Appl. Therm. Eng.* **2018**, *128*, 662–671. [CrossRef]
49. Bonato, J.L.; Perondi, D.; Manera, C.; Borghetti, M.; Ferreira, S.D.; de Almeida Neuwald, O.; Godinho, M. CO_2 adsorption evaluation of different biochars produced from peanut shell pyrolysis. *Biomass Convers. Biorefinery* **2026**, *16*, 267. [CrossRef]
50. Premchand, P.; Demichelis, F.; Chiaramonti, D.; Bensaid, S.; Fino, D. Biochar production from slow pyrolysis of biomass under CO_2 atmosphere: A review on the effect of CO_2 medium on biochar production, characterisation, and environmental applications. *J. Environ. Chem. Eng.* **2023**, *11*, 110009. [CrossRef]
51. Zhang, C.; Shan, B.; Tang, W.; Zhu, Y. Comparison of cadmium and lead sorption by Phyllostachys pubescens biochar produced under a low-oxygen pyrolysis atmosphere. *Bioresour. Technol.* **2017**, *238*, 352–360. [CrossRef] [PubMed]
52. Zhao, B.; O'Connor, D.; Zhang, J.; Peng, T.; Shen, Z.; Tsang, D.C.W.; Hou, D. Effect of pyrolysis temperature, heating rate, and residence time on rapeseed stem derived biochar. *J. Clean. Prod.* **2018**, *174*, 977–987. [CrossRef]
53. Liu, Y.; Wang, S.; Huo, J.; Zhang, X.; Wen, H.; Zhang, D.; Zhao, Y.; Kang, D.; Guo, W.; Ngo, H.H. Adsorption recovery of phosphorus in contaminated water by calcium modified biochar derived from spent coffee grounds. *Sci. Total Environ.* **2024**, *909*, 168426. [CrossRef] [PubMed]
54. Santiago, P.Q.; Silva, L.C.; Sousa, E.F.; Sousa, J.P.; Medeiros, S.L.S.; Rios, M.A.S.; Nogueira, R.E.F.Q. Structural and chemical characterization of carnauba stalk biochar (copernicia prunifera) and its application in methylene blue adsorption. *Processes* **2026**, *14*, 905. [CrossRef]
55. Li, Z.; Zhang, H.; Guo, W.; Meng, T.; Cui, H.; Ma, C. Enhanced peroxydisulfate activation by co-doping of nitrogen, chlorine, and iron: Preparation, synergistic effects, and application. *Catalysts* **2025**, *15*, 880. [CrossRef]
56. Wan, J.; Guo, Y.; Zhang, Z.; Deng, R.; Wang, X.; Cao, S.; Zhang, X.; Miao, Y.; Jiang, J.; Song, Z.; et al. Persulfate activation with biochar supported nanoscale zero- valent iron: Engineering application for effective degradation of NCB in soil. *Sci. Total Environ.* **2024**, *933*, 173053. [CrossRef] [PubMed]
57. Sher, F.; Iqbal, S.Z.; Liu, H.; Imran, M.; Snape, C.E. Thermal and kinetic analysis of diverse biomass fuels under different reaction environment: A way forward to renewable energy sources. *Energy Convers. Manag.* **2020**, *203*, 112266. [CrossRef]
58. Kim, Y.; Oh, J.-I.; Vithanage, M.; Park, Y.-K.; Lee, J.; Kwon, E.E. Modification of biochar properties using CO_2. *Chem. Eng. J.* **2019**, *372*, 383–389. [CrossRef]
59. Che, D.; Wang, L.; Liu, H.; Sun, B.; Guo, S. Effects of lipids on sludge and chlorella protein pyrolysis by thermogravimetry Fourier transform infrared spectrometry. *J. Environ. Chem. Eng.* **2022**, *10*, 107011. [CrossRef]
60. Li, X.; Cen, K.; Li, J.; Jia, D.; Gao, J.; Zhang, L.; Chen, D. Insights into the interactions between cellulose and hemicellulose during pyrolysis for optimizing the properties of biochar as a potential energy vector. *Ind. Crops Prod.* **2025**, *223*, 120126. [CrossRef]
61. Pan, Z.; Qi, G.; Zhang, X.; You, Q.; Zheng, Y.; Xiang, W.; Zhao, Y.; Gao, B. Lignin-based hierarchical porous biochar prepared from negative pressure pyrolysis enhanced CO_2 and VOCs adsorption. *Sep. Purif. Technol.* **2024**, *345*, 127398. [CrossRef]
62. Erans, M.; Arencibia, A.; Sanz-Pérez, E.S.; Sanz, R. Amine-bridged periodic mesoporous organosilica adsorbents for CO_2 capture. *J. Environ. Chem. Eng.* **2023**, *11*, 111590. [CrossRef]
63. Keiluweit, M.; Nico, P.S.; Johnson, M.G.; Kleber, M. Dynamic molecular structure of plant biomass-derived black carbon (biochar). *Environ. Sci. Technol.* **2010**, *44*, 1247–1253. [CrossRef] [PubMed]
64. Ahmad, M.; Lee, S.S.; Dou, X.; Mohan, D.; Sung, J.-K.; Yang, J.E.; Ok, Y.S. Effects of pyrolysis temperature on soybean stover- and peanut shell-derived biochar properties and TCE adsorption in water. *Bioresour. Technol.* **2012**, *118*, 536–544. [CrossRef] [PubMed]

65. Jiao, M.; Shi, Y.; Li, M.; Zhang, H.; Li, S.; Deng, H.; Xia, D. The surface functional groups-driven fast and catalytic degradation of naproxen on sludge biochar enhanced by citric acid. *Environ. Pollut.* **2024**, *361*, 124857. [CrossRef] [PubMed]
66. Tang, W.; Zanli, B.L.G.L.; Jing, F.; Hu, T.; Chen, J. Low temperature pyrolytic biochar is a preferred choice for sulfonamide-Cu(II) contaminated soil remediation in tropical climate region. *Sci. Total Environ.* **2023**, *876*, 162792. [CrossRef] [PubMed]
67. Qin, L.; Tong, T.; Huang, D.; Zhang, M.; Ma, D.; Fan, X.; Deng, H.; Lv, G.; Ma, M.; Yan, M. Efficient removal of sulfamethoxazole by boron-doped porous biochar-activated persulfate: Simultaneously enhanced adsorption and non-radical pathways. *J. Water Process Eng.* **2025**, *78*, 108708. [CrossRef]
68. Chen, Z.; Xiao, X.; Xing, B.; Chen, B. pH-dependent sorption of sulfonamide antibiotics onto biochars: Sorption mechanisms and modeling. *Environ. Pollut.* **2019**, *248*, 48–56. [CrossRef] [PubMed]
69. Zhao, J.; Zhou, D.; Zhang, J.; Li, F.; Chu, G.; Wu, M.; Pan, B.; Steinberg, C.E. The contrasting role of minerals in biochars in bisphenol A and sulfamethoxazole sorption. *Chemosphere* **2021**, *264*, 128490. [CrossRef] [PubMed]
70. Ezzati, R. Derivation of Pseudo-First-Order, Pseudo-Second-Order and Modified Pseudo-First-Order rate equations from Langmuir and Freundlich isotherms for adsorption. *Chem. Eng. J.* **2020**, *392*, 123705. [CrossRef]
71. Alves, B.S.Q.; Fernandes, L.A.; Southard, R.J. Biochar-cadmium retention and its effects after aging with Hydrogen Peroxide (H_2O_2). *Heliyon* **2021**, *7*, e08476. [CrossRef] [PubMed]
72. Diao, Y.; Shan, R.; Li, M.; Gu, J.; Yuan, H.; Chen, Y. Efficient adsorption of a sulfonamide antibiotic in aqueous solutions with N-doped magnetic biochar: Performance, mechanism, and reusability. *ACS Omega* **2023**, *8*, 879–892. [CrossRef] [PubMed]
73. Liu, B.; Xing, Z.; Xue, Y.; Zhang, J.; Zhai, J. Effect of pyrolysis temperature on the carbon sequestration capacity of spent mushroom substrate biochar in the presence of mineral iron. *Molecules* **2024**, *29*, 5712. [CrossRef] [PubMed]
74. Fan, Y.; Huang, L.; Wu, L.; Zhang, C.; Zhu, S.; Xiao, X.; Li, M.; Zou, X. Adsorption of sulfonamides on biochars derived from waste residues and its mechanism. *J. Hazard. Mater.* **2021**, *406*, 124291. [CrossRef] [PubMed]
75. Pan, B.; Xing, B. Adsorption mechanisms of organic chemicals on carbon nanotubes. *Environ. Sci. Technol.* **2008**, *42*, 9005–9013. [CrossRef] [PubMed]
76. Jiang, H.; Liu, L.; Zhao, K.; Liu, Z.; Zhang, X.; Hu, S. Effect of pyridinic- and pyrrolic-nitrogen on electrochemical performance of Pd for formic acid electrooxidation. *Electrochim. Acta* **2020**, *337*, 135758. [CrossRef]
77. Xia, W.; Liu, Y.; Tang, M.; Li, D.; Zhang, G. Meta-analysis reveals the effect of biochar on sulfonamides and tetracyclines in soil. *Sci. Rep.* **2025**, *15*, 42393. [CrossRef] [PubMed]
78. Sun, Y.; Zheng, L.; Zheng, X.; Xiao, D.; Yang, Y.; Zhang, Z.; Ai, B.; Sheng, Z. Adsorption of sulfonamides in aqueous solution on reusable coconut-shell biochar modified by alkaline activation and magnetization. *Front. Chem.* **2022**, *9*, 814647. [CrossRef] [PubMed]
79. Li, H.; Cheng, Y.; Li, F.; Wang, H.; Qing, R.; Lan, T.; Yang, Y.; Yang, J.; Liao, J.; Liu, N. Dual-template synthesis of microalgae-derived biochar for uranium removal from aqueous solution. *J. Ind. Eng. Chem.* **2025**, *148*, 560–568. [CrossRef]
80. Kayranli, B.; Bilen, M.; Seckin, I.Y.; Yilmaz, T.; Dinc, A.; Akkurt, F.; Simsek, H. Peanut shell biochar for Rhodamine B removal: Efficiency, desorption, and reusability. *Chemosphere* **2024**, *364*, 143056. [CrossRef] [PubMed]
81. Chen, W.; Wei, R.; Yang, L.; Yang, Y.; Li, G.; Ni, J. Characteristics of wood-derived biochars produced at different temperatures before and after deashing: Their different potential advantages in environmental applications. *Sci. Total Environ.* **2019**, *651*, 2762–2771. [CrossRef] [PubMed]
82. Wang, C.; Chen, W.; Yang, L.; Wei, R.; Ni, J.; Yang, Y. Insights into the roles of the morphological carbon structure and ash in the sorption of aromatic compounds to wood-derived biochars. *Sci. Total Environ.* **2019**, *693*, 133455. [CrossRef] [PubMed]
83. Guo, J.; Zheng, L.; Li, Z.; Zhou, X.; Cheng, S.; Zhang, L.; Zhang, Q. Effects of various pyrolysis conditions and feedstock compositions on the physicochemical characteristics of cow manure-derived biochar. *J. Clean. Prod.* **2021**, *311*, 127458. [CrossRef]
84. *GB/T 212-2008*; Proximate Analysis of Coal. China Standards Press: Beijing, China, 2008.
85. Hafner, J. Ab-initiosimulations of materials using VASP: Density-functional theory and beyond. *J. Comput. Chem.* **2008**, *29*, 2044–2078. [CrossRef] [PubMed]
86. Blöchl, P.E. Projector augmented-wave method. *Phys. Rev. B* **1994**, *50*, 17953–17979. [CrossRef] [PubMed]
87. Perdew, J.P.; Burke, K.; Ernzerhof, M. Generalized gradient approximation made simple. *Phys. Rev. Lett.* **1996**, *77*, 3865–3868. [CrossRef] [PubMed]
88. Grimme, S. Semiempirical GGA-type density functional constructed with a long-range dispersion correction. *J. Comput. Chem.* **2006**, *27*, 1787–1799. [CrossRef] [PubMed]
89. Monkhorst, H.J.; Pack, J.D. Special points for Brillouin-zone integrations. *Phys. Rev. B* **1976**, *13*, 5188–5192. [CrossRef]
90. Kwon, Y.; Kim, S.; Moon, S.; Yum, J.; Shin, J.; Kwak, J.; Jun, B.-M.; Chon, K. Enhanced adsorption of pharmaceuticals using coffee ground biochars via $KHCO_3$ and urea pre-treatment: Effects of π-π interactions and hydrogen bonding. *Environ. Chem. Ecotoxicol.* **2027**, *9*, 92–103. [CrossRef]
91. Nguyen, V.-T.; Nguyen, T.-B.; Huang, C.P.; Chen, C.-W.; Bui, X.-T.; Dong, C.-D. Alkaline modified biochar derived from spent coffee ground for removal of tetracycline from aqueous solutions. *J. Water Process Eng.* **2021**, *40*, 101908. [CrossRef]

92. Maged, A.; Dissanayake, P.D.; Yang, X.; Pathirannahalage, C.; Bhatnagar, A.; Ok, Y.S. New mechanistic insight into rapid adsorption of pharmaceuticals from water utilizing activated biochar. *Environ. Res.* **2021**, *202*, 111693. [CrossRef] [PubMed]
93. Huyen, V.L.D.; Nguyen, T.H.; Truong-Lam, H.S. Phosphoric-acid-activated biochar derived from spent coffee grounds as sustainable adsorbent for solid-phase extraction. *Mater. Today Commun.* **2026**, *54*, 115590. [CrossRef]
94. Yoon, K.; Kwon, G.; Kim, E.; Lee, H.; Lee, D.-J.; Song, H. Pyrolytic conversion of cattle manure into value-added products and application of biochar for adsorption of sulfamethoxazole. *Chemosphere* **2024**, *366*, 143493. [CrossRef] [PubMed]
95. Lin, S.; Shen, Z.; Pan, D.; Ji, R.; Bian, Y.; Han, J.; Jiang, X.; Song, Y.; Cheng, H.; Xue, J. Marine macroalgae-derived multielement-doped porous biochars for efficient removal of sulfamethoxazole from aqueous solution: Sorption performance and governing mechanisms. *J. Anal. Appl. Pyrolysis* **2023**, *171*, 105963. [CrossRef]
96. Huang, J.; Zimmerman, A.R.; Chen, H.; Gao, B. Ball milled biochar effectively removes sulfamethoxazole and sulfapyridine antibiotics from water and wastewater. *Environ. Pollut.* **2020**, *258*, 113809. [CrossRef] [PubMed]
97. Huang, J.; Zimmerman, A.R.; Chen, H.; Wan, Y.; Zheng, Y.; Yang, Y.; Zhang, Y.; Gao, B. Fixed bed column performance of Al-modified biochar for the removal of sulfamethoxazole and sulfapyridine antibiotics from wastewater. *Chemosphere* **2022**, *305*, 135475. [CrossRef] [PubMed]

Disclaimer/Publisher's Note: The statements, opinions and data contained in all publications are solely those of the individual author(s) and contributor(s) and not of MDPI and/or the editor(s). MDPI and/or the editor(s) disclaim responsibility for any injury to people or property resulting from any ideas, methods, instructions or products referred to in the content.